Journal of the Islamic University of Gaza, (Natural Sciences Series) Vol..12, No.1, PP. 123-152, 2004

An Improved Graphical Visualization for the Subsonic-Steady Aerodynamic of Delta Wings Using MATLAB

Jamal M. Elzebda, Civil Engineering Department, The Islamic University of Gaza (IUG) Email: jelzebda@mail.iugaza.edu

Abstract The MATLAB programming language is used to write a generalized computer code to numerically simulate the aerodynamic of a lifting surface using the general vortex-lattice method. This code is used to model the flowfield and predict the aerodynamic loads. The subsonic, steady aerodynamic of a delta wing is used as an example. The powerful graphical tools of MATLAB are used to produce the following: 3-D visualizations of the wakes with/without hidden-line removal, the roll-up of the leading edge wakes, the propagation of the convected vortices, and 3-D pressure distributions. The results obtained in the present work support the physical interpretations of the wing-rock phenomenon and the multi-surface interference previously investigated by many authors; yet with significant improvement on the graphical visualizations.

1. Introduction

Aerodynamic modeling of lifting surfaces is a problem of long-standing interest and one about which much has been written. Because the vortex-lattice method (VLM) provides both aerodynamic loads and wakes as parts of the solution, it appears to be the most promising analytical/numerical method for treating subsonic flows over arbitrary lifting surfaces. VLM is not limited to planform, angle of attack, camber or twist as long as vortex bursting does not occur in the near vicinity of the configuration and separation occurs only along known lines.

There have been many efforts to investigate and understand the subsonic aerodynamic of lifting surfaces using the steady/unsteady VLM:

a) Steady aerodynamic of a single surface with arbitrary planform [1]:
   In this work, the author numerically simulated the steady subsonic aerodynamic of a delta wing at different angles of attack obtaining aerodynamic coefficients and the corresponding flowfields.
b) One-degree-of-freedom wing-rock of delta wings [2, 3]:
   In this study, the authors combined the unsteady VLM with a predictor-corrector integration scheme to simultaneously predict the flowfield and the motion of the wing, which is caused by the aerodynamic loads acting on it. Their results are in good agreement with the experimental results of Nguen et al [4] and compare well with those of Levin and Katz.[5].

c) Two-degree-of-freedom wing-rock of delta wings [1, 6]:
   In this investigation, the authors combined the unsteady VLM with the predictor-corrector scheme to simulate the wing rock of delta wings for the cases: one degree of freedom in roll, one degree of freedom in pitch, and two degrees of freedom in roll and pitch. These cases addressed different angles of attack with certain initial disturbance. The results (amplitude and period of the limit-cycle motion) for one degree of freedom in roll agreed closely with the observations of Levin and Katz [5]. For one degree of freedom in pitch, the motion was always found to decay to the static equilibrium position. For the two degrees of freedom, the simulation resulted in two critical angles of attack. For angles of attack below the first critical angle, all initial perturbations decay and the wing is stable. For angles of attack between the two critical ones, the oscillation in pitch becomes very small, but a large-amplitude limit cycle develops in roll. For angles of attack greater than the second critical angle, all initial disturbances lead to large-amplitude motions in both roll and pitch. No wind-tunnel tests have been conducted to verify the results for the case of two degrees of freedom.
d) Modeling the flows over an arbitrary number of lifting surfaces [7, 8]:
   In this work, the authors extended the unsteady VLM to simulate the flows over an arbitrary number of lifting surfaces. The X-29A (two canards and forward sweep main wing) was used as a model, and simulations of the steady and unsteady aerodynamic interference were presented. The results for the steady aerodynamic agreed closely with wind-tunnel data [9], and the results for the unsteady one agreed with the wind-tunnel data given by reference [10]. Results for unsteady interference due to motion of the canards have been obtained, i.e.; the strong influence of the canards on the main wing including the pressure distributions.

As far as the author is aware, all previous studies ***produced precise numerical results*** for the different aerodynamic load coefficients, however; ***not enough efforts have been made to obtain clear graphical visualizations*** of the flowfields over the lifting surfaces. In the present paper, powerful and high-level graphics tools are used to overcome this deficiency.

2. Description of the Numerical Model (Vortex-Lattice Method)

In this section, the problem of subsonic-steady aerodynamic is briefly described. For a complete description of the VLM, the reader is referred to Chapter II of reference [1].

2.1 Coordinate systems, Position and Rotations

In Figure 1, we show a typical wing and two coordinate systems. The coordinates systems are used as follows:

a) (X Y Z) which is an inertial frame of reference called ground-fixed (G-F) or global frame.
b) (x y z) which is a moving frame of reference attached to the wing called body-fixed (B-F) or local frame.

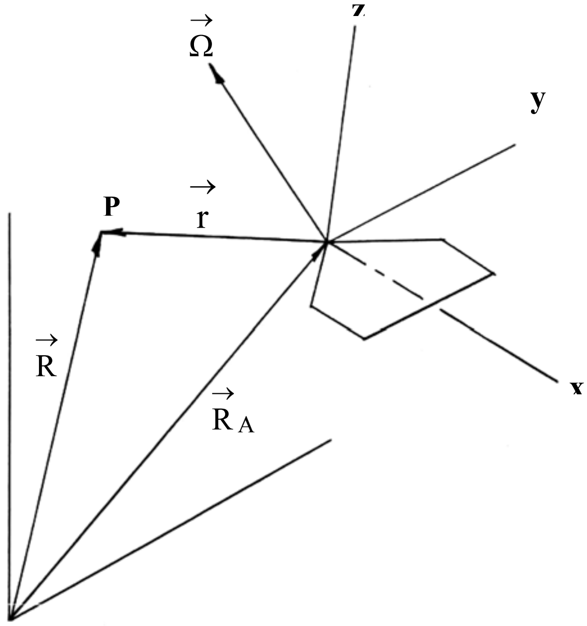

Figure 1. Two coordinate systems:
Global ground-fixed (XYZ) & Local body-fixed (xyz)

The motion of the wing has, in general, six degrees of freedom (6 independent functions of time):

a) three components of the position vector of the origin of the moving B-F frame, and

b) a set of three Euler angles (ξ, θ, ψ).

The B-F frame is viewed as being originally aligned with the G-F frame. Then the B-F frame undergoes the following sequence:

a) a yaw-like rotation (ψ) about the original z-axis, followed by
b) a pitch-like rotation (θ) about the new y-axis, followed by
c) a roll-like rotation (ξ) about the new x-axis.

The unit vectors in the G-F frame $(\vec{I}, \vec{J}, \vec{K})$ are related to those in the B-F $(\vec{i}, \vec{j}, \vec{k})$ frame as follows:

$$\begin{Bmatrix} \vec{i} \\ \vec{j} \\ \vec{k} \end{Bmatrix} = [C] \begin{Bmatrix} \vec{I} \\ \vec{J} \\ \vec{K} \end{Bmatrix} \quad \text{and} \quad \begin{Bmatrix} \vec{I} \\ \vec{J} \\ \vec{K} \end{Bmatrix} = [C]^T \begin{Bmatrix} \vec{i} \\ \vec{j} \\ \vec{k} \end{Bmatrix} \tag{1}$$

where

$$[C] = \begin{bmatrix} C\theta\, C\psi & C\theta\, S\psi & -S\theta \\ S\xi\, S\theta\, C\psi - C\xi\, S\psi & S\xi\, S\theta\, S\psi + C\xi\, C\psi & S\xi\, C\theta \\ C\xi\, S\theta\, C\psi + S\xi\, S\psi & C\xi\, S\theta\, S\psi - S\xi\, C\psi & C\xi\, C\theta \end{bmatrix} \tag{2}$$

and **C** and **S** denote the cosine and sine functions, respectively.

From Figure 1, the position of an arbitrary point P can be expressed, in the G-F frame, as follows:

$$\vec{R} = \vec{R}_A + \vec{r} \tag{3}$$

where $\vec{R}_A$ is the position of the origin A of the B-F frame in the G-F frame, and $\vec{r}$ is the position of point P relative to the B-F frame.
Differentiation of Equation (3) yields

$$\vec{V} = \vec{V}_A + \vec{\Omega} \text{ x } \vec{r} + \vec{v} \tag{4}$$

where $\vec{V}$ is the velocity of point P in the G-F frame, $\vec{V}_A$ is the velocity of the origin A of the B-F frame in the G-F frame, $\vec{\Omega}$ is the angular velocity of the

B-F frame, and $\vec{v}$ is the relative velocity of point P in the B-F frame. For points fixed in the surface of the wing, the velocity relative to the B-F frame is zero; therefore,

$$\vec{V} = \vec{V}_A + \vec{\Omega} \times \vec{r} \qquad (5)$$

The motion of the wing is specified by the vector functions $\vec{V}_A(t)$ and $\vec{\Omega}(t)$. Typically, we specify $\vec{\Omega}(t)$ through Euler angles and their derivatives. In other words, if the angular velocity of the wing is written as

$$\vec{\Omega} = \Omega_x \vec{i} + \Omega_y \vec{j} + \Omega_z \vec{k} \qquad (6)$$

then the components in Equation (6) are related to the derivatives of the Euler angles as follows:

$$\begin{Bmatrix} \Omega_x \\ \Omega_y \\ \Omega_z \end{Bmatrix} = [B] \begin{Bmatrix} \dot{\psi} \\ \dot{\theta} \\ \dot{\xi} \end{Bmatrix} \qquad (7)$$

where

$$[B] = \begin{bmatrix} -S\theta & 0 & 1 \\ S\xi\, C\theta & C\xi & 0 \\ C\xi\, C\theta & -S\xi & 0 \end{bmatrix} \qquad (8)$$

2.2 Simulating the Wing and its Wake

As the lifting surface moves, it creates a disturbance and sets the air in motion. As a result of viscosity in the real fluid, vorticity is generated in the boundary layers on the upper and lower surfaces and vortices are formed along the sharp edges. These vortices are shed and convected away from the wing, and form the wake. In the numerical model all the vorticity in the flow is restricted to a thin region around the lifting surface and its wake, and the flow outside this region is considered irrotational. The wing and its wake are approximated by a sheet of vorticity which consist of two parts:

a) The bound vortex sheet that represents the wing whose position is specified. Specifying the position of the vortex sheet, in general, produces a difference in the pressures on the two sides of the sheet. This difference is the basis for predicting the aerodynamic loads on the wing.

b) The free vortex sheet that represents the wake whose position is not specified a priori; it is allowed to deform freely during the motion until it assumes a force-free position. As a result, there is no pressure jump across it. The position of this sheet is obtained as part of the solution.

The two parts of the vortex sheet are joined along the sharp edges where separation occurs, the same edges where Kutta condition is imposed in a steady flow. In the numerical model, a lattice of discrete vortex lines represents the vortex sheet. Subsequently, we consider the use of lattices of discrete vortex segments to simulate the lifting surface and its wake. Each segment in the lattices is a straight segment. Figure 2 shows the evolution of the numerical model from wing to vortex lattice.

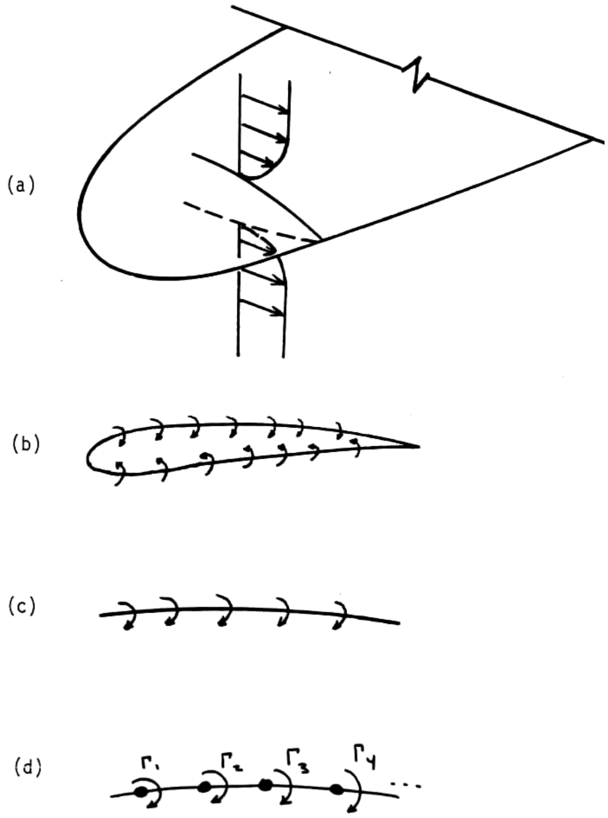

Figure 2. The evolution of the numerical mode:
(a) Actual boundary layers, exaggerated.
(b) Profile of upper and lower boundary layer presented by vortex sheets.
(c) Upper and lower vortex sheets merged on the surface to form a "lifting surface".
(d) The single vortex sheet on the surface represented by a lattice of discrete vortex lines (called vortices).

The velocity field generated by a single straight vortex segment is obtained using the Biot-Savart law [15]:

$$\vec{V} = \frac{\Gamma}{4\pi h}(\cos\theta_A - \cos\theta_B)\,\vec{e}_v \qquad (9)$$

The terms in Equation (9) are identified in Figure 3: Γ is the circulation around the vortex segment, which extends from point A to point B with positive sense according to the right-hand rule. The parameter h is the distance from point P, where the velocity is being determined, to the line defined by points A and B. The angles θ_A and θ_B are defined in the figure. The unit vector $\vec{e}_v$ is perpendicular to the plane defined by the three points – A, B, and P – and is in the direction of $\vec{\omega} \times \vec{r}_1$, where both $\vec{\omega}$ (the vorticity) and $\vec{r}_1$ (the position of point P relative to point A) are shown in the figure. Equation (9) is considered the fundamental building block of the vortex-lattice method.

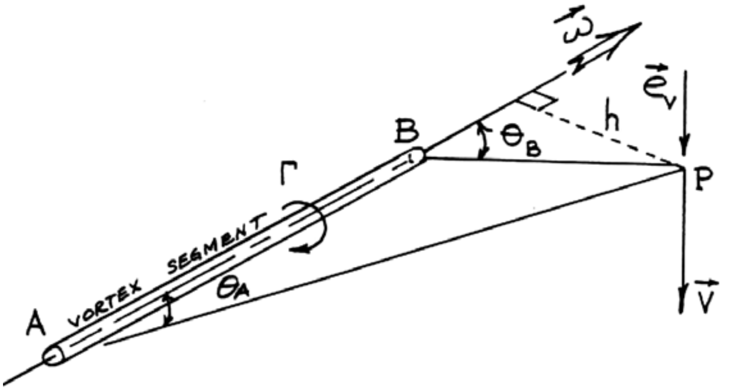

Figure 3. A straight segment of a discrete vortex line. The velocity induced by this segment at point P is given Equation (9).

2.3 Governing Equations for the Circulations Around the Discrete Vortex Segments

2.3.a Spatial Conservation of Circulation

One of the results of the Kelvin-Helmoltz theory of vorticity is that at any instant the circulation a round a vortex line is constant [15]. This implies that vortex lines never end. To satisfy this requirement the vortex lattice is made of closed loops of constant-circulation vortex lines. These loops enclose the elements of area that make up the bound lattice and the free lattice. Typical loops in the bound and free lattices of a rectangular planform are shown in Figure 4. One such loop is ACDBA, having the circulation G_2 around each of its four vortex segments. The segments AB abd BD are common to two loops in the bound lattice; consequently, the circulations around these segments are G_1-G_2 and G_4-G_2, respectively.

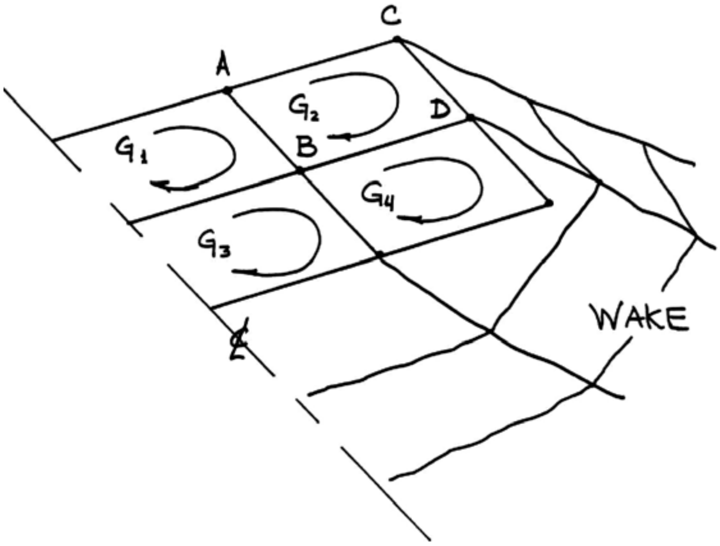

Figure 4. A schematic representation of a bound and a free vortex lattice. G_1, G_2, G_3, and G_4 are the values of the circulations around the closed loops of vorticity that form the bound lattice.

2.3.b Infinity Condition

The disturbances created by the wing and its wake must decay as the distances from them increases. Because the disturbance velocity is computed according to the Biot-Savart law, Equation (9), this requirement is satisfied.

2.3.c No-Penetration Condition

The fluid particles do not penetrate the surface of the wing; thus, we set the normal component of the relative velocity equal to zero:

$$(\vec{V} - \vec{V}_{LS}) \cdot \vec{n} = 0 \qquad \text{on} \qquad S_{LS} \qquad (10)$$

where $\vec{V}$ is the absolute velocity of the fluid particle in contact with the lifting surface, $\vec{V}_{LS}$ is the velocity of the contact point in the lifting surface

(computed from Equation 5), S_{LS} denotes the lifting surface and $\vec{n}$ is the normal unit vector where the no-penetration condition is being satisfied. The points where Equation (10) is imposed, called control points, are the centroids of the corners of the rectangular elements and the midpoints of the hypotenuses of the triangular elements along the edges of delta wings.
The velocity of the fluid particle is the sum of two contributions:

$$\vec{V} = \vec{V}_B + \vec{V}_F \qquad (11)$$

where $\vec{V}_B$ is the velocity induced by the bound lattice (wing) and $\vec{V}_F$ is the velocity induced by the free lattice (wake). Upon substituting Equation (11) into Equation (10), we obtain

$$\begin{gathered}(\vec{V}_B \cdot \vec{n})_i = [(\vec{V}_{LS} - \vec{V}_F) \cdot \vec{n}]_i \\ \text{for} \quad i = 1, 2, \cdots, N\end{gathered} \qquad (12)$$

Here **i** denotes the number of the element and **N** is the total number of elements in the lifting surface. One equation is written for each element and evaluated at the control point of the element.

The normal component of the velocity $\vec{V}_B$ at the control point of the element **i** is expressed as follows:

$$(\vec{V}_B \cdot \vec{n})_i = \sum_{j=1}^{N} A_{ij} G_i \qquad (13)$$

where A_{ij} is the normal component of the velocity induced at the control point of element **i** by the vortex loop of circulation 4π around element **j**. Substituting Equation (13) into Equation (12) leads to

$$\sum_{j=1}^{N} A_{ij} G_j = [(\vec{V}_{LS} - \vec{V}_F) \cdot \vec{n}]_i \quad for \quad i = 1, 2, \cdots, N \qquad (14)$$

This equation is used to obtain the unknown circulations G_j. Of course, in the computer code, we have to provide $\vec{V}_{LS}$ (Equation 5) and the velocity induced by the wake ($\vec{V}_F$) which is computed from previous steps or from initial conditions. Next we evaluate the influence coefficient matrix A_{ij}, and finally we solve for the unknown G_j.

2.3.d The Unsteady Kutta Condition, the Temporal Conservation of Circulation, and the Formation of the Wake

Spatial conservation of circulation dictates that there must be a discrete vortex along the leading and trailing edges. The goal, here, is to force the difference in the pressures on the upper and lower surfaces to vanish along the leading and trailing edges. The imposed condition that causes this goal is called the Kutta condition; stated as follows:

In an unsteady flow, all vorticity along the edges where Kutta condition is applied in a steady flow are shed into the flow field. In the case of delta wings the vortex segments extending from the leading edge into the flowfield are in the plane of the leading-edge element and are perpendicular to the leading edge [16, 17]

Because the pressure is continuous in the wake where viscous effects are negligible, the Kelvin-Helmoltz theory of vorticity [15] requires that the circulation around any given loop of the fluid particles does not change with time as these particles are convected in the flow:

$$\frac{D\Gamma}{Dt} = 0 \qquad \text{on} \quad S_W \tag{15}$$

where $\frac{D}{Dt}$ denotes the substantial (material or co-moving) derivative. To satisfy this requirement, the present method computes the velocity at each node and then displaces the nodes according to

$$\begin{aligned} \vec{r}(t+\Delta t) &= \vec{r}(t) + \vec{v}(t)\,\Delta t \\ &= \vec{r}(t) + [\vec{V}(t) - \vec{V}_A(t) - \vec{\Omega}(t) \text{ x } \vec{r}(t)]\,\Delta t \end{aligned} \tag{16}$$

where $\vec{r}(t)$ is the current position of the node, $\vec{v}(t)$ is the current velocity at the current position relative to the moving frame (see Eq. 4), and $\vec{r}(t+\Delta t)$ is the position of the node at the next time step. Using Equation (16) for all nodes in the wake will produce the change in the position of the wake relative to the B-F frame.

2.4 Special Parameters

There are some parameters that vortex-lattice codes must incorporate in order to avoid singularities or other physically untenable predictions. These modeling guidelines are:

a) Cuttoff length:
To avoid any singularity when using the Biot-Savart law (Equation 9), we provide a length so that when h is less than this length the velocity field is set to zero. Usually this cutoff length is provided in terms of the vortex segment. The value (0.1*length of vortex segment) has shown best results.

b) Leading-Edge Extension:
Experience has shown that accurate results and robust convergence as the number of elements increase can be obtained when the vortex segments extending from the leading edge into the flow are perpendicular to the edge, in the plane of the delta wing, and equal in length to the spanwise dimension of one of the rectangular elements.

c) Prevention of Penetration of the Lifting Surface by Leading-edge Vortex lines:
When several rows are used in the bound surface mesh, there is a possibility that one of the vortex lines representing the wake may curve sharply and penetrate the surface of the wing. This is possible because the no-penetration condition is satisfied at only the control points. A statement has been added to the computer code that does not permit any point in the wake to get closer to the lifting surface than some prescribed value. This value is called Dsafe (safe distance). This length is usually specified in terms of the chord; the value (0.05*chord) has shown good convergence of loads.

d) Dimensionless Variables and Uniformity Between Time Steps and Mesh Size:
It is convenient to introduce dimensionless variables (denoted by asterisks):

$$\vec{v}^{\,*} = \frac{\vec{v}}{U_c}\ ,\quad \vec{r}^{\,*} = \frac{\vec{r}}{L_c} \quad \text{and} \quad t^* = \frac{U_c}{L_c}t \qquad (17)$$

where U_c and L_c are the characteristic speed and length, respectively. Here, U_c is the forward speed of the wing; or the speed of the air when the wing is viewed as a stationary body. And L_c is the chordwise length of the rectangular elements in the bound lattice. In addition, the equation

$$\vec{v} = \vec{V} - \vec{V}_A - \vec{\Omega} \times \vec{r}$$

may be written using dimensionless variables as

$$\vec{v}^{\,*} = \vec{V}^{\,*} - \vec{V}_A^{\,*} - \vec{\Omega}^{\,*} \times \vec{r}^{\,*} \tag{18}$$

where
$$\vec{\Omega}^{\,*} = \frac{L_c}{U_c}\vec{\Omega} \quad , \quad \vec{V}_A^{\,*} = \frac{\vec{V}_A}{U_c} \tag{19}$$

Experience has shown that the vortex lattice method yields the best results when the elements in the bound and free lattices are nearly uniform. This is accomplished by choosing the time step in dimensionless variables to be unity. So, reconsidering Equation (16), which is used to convect nodes in the wakes and which determines the lengths of the elements in the wake:

$$\vec{r}(t+\Delta t) = \vec{r}(t) + \vec{v}(t)\,\Delta t$$

in dimensionless variables this can be written as follows

$$\vec{r}^{\,*}(t+\Delta t) - \vec{r}^{\,*}(t) = \vec{v}(t)^{*}\,\Delta t^{*} \tag{20}$$

where $\vec{v}^{\,*}$ is near unity as a result of the definition of the characteristic speed; consequently, $\vec{r}^{\,*}(t+\Delta t) - \vec{r}^{\,*}(t)$ is also near unity when Δt^{*} is unity.

To this end, one should be able to use the tools introduced so far to calculate the circulations and compute the flowfields for subsonic steady motion of a delta wing given an impulsive start (see examples in section 5).

2.5 Aerodynamic Loads

The loads are obtained from Bernoulli's equation. The difference in pressures on the upper and lower surfaces at the control points of the elements is first calculated. This pressure difference is multiplied by the area of the element; the result is a force normal to the element acting through the control point. These forces are then combined to produce force and moment coefficients. Starting with Bernoulli's equation form for unsteady flows:

$$\left.\frac{\partial \phi}{\partial t}\right|_{\vec{R}} + \frac{V^2}{2} + \frac{P}{\rho} = H(t) \tag{21}$$

where ϕ is the velocity potential, V is the magnitude of the velocity in the G-F frame, P is the pressure, ρ is the density, H is a spatially uniform function of time, and $\left.\frac{\partial \phi}{\partial t}\right|_{\vec{R}}$ is the partial derivative holding the position in the G-F frame, $\vec{R}$, constant.

Considering the spatial and temporal derivatives of ϕ, and the Bernoulli's equation for the B-F frame in dimensionless form, Equation (21) may yield to the pressure coefficient in the form

$$C_P = \frac{P_\infty - P}{\frac{1}{2}\rho U_c^2} = 2\frac{\partial \phi^*}{\partial t^*} + \vec{V}^* \cdot \vec{V}^* - 2(\vec{V}_A^* + \vec{\Omega}^* \times \vec{r}^*) \cdot \vec{V}^* \qquad (22)$$

where P_∞ is the pressure far from the wing and its wake, where the fluid is at rest, and

$$\phi^* = \frac{\phi}{U_c L_c} \quad , \quad \vec{V}_A^* = \frac{\vec{V}_A}{U_c} \quad , \quad \vec{V}^* = \frac{\vec{V}}{U_c} \quad , \quad \vec{\Omega}^* = \frac{L_c}{U_c}\vec{\Omega} \quad ,$$

$$\vec{r}^* = \frac{\vec{r}}{L_c} \quad \text{and} \quad t^* = \frac{U_c}{L_c} t$$

where U_c, L_c, and (U_c/L_c) are the characteristic speed, length, and time.

The dimensionless difference between the pressures on the lower and upper surfaces (i.e., pressure jump) at a control point i is given by:

$$\Delta C_{P\,i} = \frac{P_\ell - P_u}{\frac{1}{2}\rho U_c^2} = 2\frac{\partial}{\partial t^*}(\phi_u^* - \phi_\ell^*) + (\vec{V}_u^* \cdot \vec{V}_u^* - \vec{V}_\ell^* \cdot \vec{V}_\ell^*)$$
$$+ 2(\vec{V}_\ell^* - \vec{V}_u^*) \cdot (\vec{V}_A^* + \vec{\Omega}^* \times \vec{r}^*) \qquad (23)$$

Considering the local discontinuity by the vortex sheet and expressing the term $(\phi_u^* - \phi_\ell^*)$ in terms of the loop circulations (the G's), which can be related to a line integral and hence evaluated using Stokes' theorem, we can rewrite Equation (23) as

$$\Delta C_{P\,i} = 2\frac{\partial G_i^*}{\partial t^*} + 2\,\Delta\vec{V}^* \cdot (\vec{V}_m^* - \vec{V}_A^* - \vec{\Omega}^* \times \vec{r}^*) \qquad (24)$$

where $\overset{\rightarrow *}{V_m}$ is the velocity generated by all the vortex segments at the ith control point, and $\Delta \overset{\rightarrow *}{V}$ is the local discontinuity created by the vortex sheet expressed in terms of the circulations around the element. And finally the term $(\partial G_i / \partial t)$ is evaluated using a two-point finite-difference formula:

$$\frac{\partial G_i}{\partial t}(t) = \frac{G_i(t) - G_i(t - \Delta t)}{\Delta t} \qquad (25)$$

Equation (24) provides the pressure jump across the surface at the control point i. Assuming cambered surface, we can use this equation to obtain the elemental force vector:

$$\overset{\rightarrow}{F_i} = \Delta C_{P\,i} \cdot A_i \overset{\rightarrow}{n_i} \qquad (26)$$

where A_i is the element area and $\overset{\rightarrow}{n_i}$ is the unit normal vector of element i. Equation (26) can be rewritten as

$$\overset{\rightarrow}{F_i} = F_{xi} \vec{i} + F_{yi} \vec{j} + F_{zi} \vec{k} \qquad (27)$$

Summing the z-component of all forces, the normal-force coefficient can be defined as

$$CN = \frac{\sum_{i=1}^{N} F_{zi}}{S} \qquad (28)$$

where N is the total number of surface elements and S is the plan area of the surface.

Next we introduce Equation (27) in G-F frame

$$\overset{\rightarrow}{F_i} = \begin{Bmatrix} F_{xi} \\ F_{yi} \\ F_{zi} \end{Bmatrix}^T \begin{Bmatrix} \vec{i} \\ \vec{j} \\ \vec{k} \end{Bmatrix} = \begin{Bmatrix} F_{xi} \\ F_{yi} \\ F_{zi} \end{Bmatrix}^T [C_n] \begin{Bmatrix} \vec{I} \\ \vec{J} \\ \vec{K} \end{Bmatrix}$$

or

$$\vec{F}_i^{\,G} = \begin{Bmatrix} F_{xi}^G \\ F_{yi}^G \\ F_{zi}^G \end{Bmatrix}^T \begin{Bmatrix} \vec{I} \\ \vec{J} \\ \vec{K} \end{Bmatrix} \tag{29}$$

where the superscript G implies forces are in the G-F frame. Again, summing over all surface elements, the drag and the lift coefficients are defined as

$$CD = \frac{\sum_{i=1}^{N} F_{xi}^G}{S} \quad \text{and} \quad CL = \frac{\sum_{i=1}^{N} F_{zi}^G}{S} \tag{30}$$

Finally, using Equation (27), the moment-coefficients vector can be defined as follows

$$\vec{CM} = \frac{\sum_{i=1}^{N} \vec{r}_i \times \vec{F}_i}{SC} \tag{31}$$

where $\vec{r}_i$ is the vector connecting the control point i and the point about which the moment is taken (usually the origin of the wing) and C is the chord. Equation (31) can be written as

$$\vec{CM} = CMR\,\vec{i} + CMP\,\vec{j} + CMY\,\vec{k} \tag{32}$$

where CMR, CMP, and CMY are the rolling-moment, pitching-moment, and yawing-moment coefficients, respectively.

3. MATLAB in Lines [11, 12, 13, 14]

The codes used in the numerical simulations discussed in section 1 were written using Fortran computer-programming language. In the present study, the strong matrix manipulations and graphical abilities of the high-technical programming language MATLAB are used.

MATLAB is a high-performance programming language for technical computing. It integrates computation, visualization, and programming in an easy-to-use environment.

MATLAB, like any other programming languages, provides many low-level and high-level programming tools. Some of the features that MATLAB provides start from simple arithmetic operations to flow controls and all the way to class and object manipulations. At the graphics level, MATLAB provides features of simple 2-D plotting, image processing, 3-D models, and all the way to animations and movies.

The strong matrix manipulations of MATLAB are used to write a new source code to numerically simulate the subsonic aerodynamic for any arbitrary planform. In other words, the code computes the flow flowfields and calculates the aerodynamic loads. The powerful and sophisticated graphics tools of MATLAB are then used to significantly improve the graphical visualization of the subsonic aerodynamic of delta wings.

4. Conversion and Major Enhancements of Older Source-Code Versions

In the previous studies discussed in section 1, the computer source codes written in Fortran have produced great results. However, the evolution of powerful high-performance computational programming languages, such as MATLAB, helped to discover some disadvantages in those older code versions. Some of these disadvantages are:

1) Long source codes (for example, about 2 thousands code lines to simulate the subsonic aerodynamics of delta wings).
2) Different versions of basically the same code; each version treated a specific planform, i.e.; one had to use a code to simulate rectangular wings, another code to simulate delta wings, and so on.
3) For a given planform, changing the size of the bound-surface mesh or the order of the elements in the mesh (4 or 5 sides, for example) meant lengthy modifications in the code. For example, for rectangular wings, only fourth order (4 sides) elements were used. But if for some reason a higher order element needed to be used, complicated modifications had to be introduced in the code.
4) The bound-surface mesh for delta wings was limited to the fact that the number of columns is always equal to twice the number of rows. This limitation produced slender elements on the bound surface, which created very slender elements in the wake (trailing edge wake, in particular) and hence, sometimes, produced unnecessary high values of the velocity.
5) Primitive graphics subroutines (functions), which produced poor graphical presentations of flowfields over lifting surfaces.

In the present investigation, the source code of the subsonic-steady aerodynamic for a single lifting surface is rewritten using MATLAB and hence leading to the following enhancements:

1) Short source codes (about one-half of the old code, for example, about 1100 code lines to simulate the subsonic aerodynamics of delta wings).
2) Implementing the "incident matrix" concept helped to develop a ***most general and flexible*** code to predict aerodynamic loads for any arbitrary lifting surface using the VLM. This code is so general and flexible; it is not limited to any specific shape or planform**.** When using the "incident matrix" idea, one simply assigns certain characteristics for a node, a vortex segment, and for a mesh element. This results in a quick and simple retrieving and access of such characteristics whenever needed. Such matrices lead us to develop one version of code to treat different planforms (rectangular, delta, …).
3) Simplicity of changing the size of the bound-surface mesh.
4) A complete freedom to select the order, orientation, and shape of the elements in the bound-surface mesh.
5) Very powerful graphical techniques used to produce clear and improved graphical visualization of flowfields over lifting surfaces.

The only disadvantage that comes with this general version of the code is inputting the data which proven to be a cumbersome task, i.e.; it takes a long time to type in the special characteristics of the nodes, vortex segments, and mesh elements.

5. Computations using the New Source-Code Version

5.1 Numerical Results

The new code version (MATLAB version) is used to simulate the steady aerodynamic of a delta wing with aspect ratio of one. To obtain a steady flow, we first give the configuration an impulsive start, and then have it translate at constant velocity until steady state develops. Computations were made using two bound-surface meshes (3 rows and 6 rows of elements in bound surface mesh) at three different angles of attack. Figure 5 shows the bound surface lattice along with the control points for 6 rows.

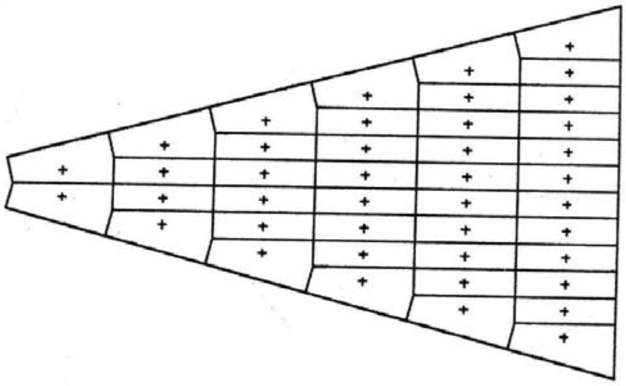

Figure 5. Bound lattice used in calculations (6 rows)

Numerical results obtained here are in full agreement with those results obtained using the old Fortran version [1]. Table 1 shows the steady-state values of normal-force coefficient (**CN**) and pitch-moment coefficient (**CMP**) for different angles of attack (**α**) and different bound-surface meshes (3 rows and 6 rows).

Table 1. Aerodynamic Coefficients

Rows	Nwakes*	Nsteps**	$\alpha = 10^o$		$\alpha = 15^o$		$\alpha = 20^o$	
			CN	CMP	CN	CMP	CN	CMP
3	8	11	0.2557	-0.1394	0.4549	-0.2419	0.6859	-0.3548
6	15	21	0.3321	-0.1935	0.5420	-0.3158	0.7866	-0.4516

* Nwakes = Number of wake segments used.
** Nsteps = Number of time steps used.

It should be mentioned that, for both cases in table 1, the following values were used:

Minimum distance between bound surface and the wake vortex segments

= 0.05 * chord - (used when convecting the wake segments).

Cutoff lengths in the bound and wake lattices

= 0.1 * length of vortex segment - (used in Biot-Savart Law).

Now we have proven that the new MATLAB version of the code can produce *exactly the same numerical results* obtained by older code versions, we are ready to show how the new Code enhances the graphical results.

5.2 Graphical Results

To ensure a complete formation of the steady state flowfields, the computations conducted in section 5.1 are repeated here but with both the number of wake segments (parallel to flight direction) and the number of time steps being increased. Some computations took 35-40 minutes on a Pentium 4 PC.

5.2.a Computing flowfields with/without hidden-line removal

Figure 6 shows the steady-state results of the flowfield at angle of attack $\boldsymbol{\alpha} = \mathbf{20^o}$**,** number of wake segments (Nwakes) = 18, and number of time steps (Nsteps) = 30.

Figure 6a shows the top view of the flowfield over the wing without and with hidden-line removal. Similarly, Figure 6b shows the side views and 6c shows the end views. The views with hidden-line removal show a ***more complete and clearer visualization*** of the total flowfield than those views that depicted without hidden-line removal (as would have been produced by older code versions). Roll up of leading-edge wakes and their penetrations of the trailing-edge wakes are also very clear.

5.2.b Propagation of an impulsive-start vortices

Computations of section 5.2.a are repeated for angle of attack $\boldsymbol{\alpha} = \mathbf{20^o}$**,** number of wake segments Nwakes = 18, but with different times steps (Nsteps = 21, 24, 27, and 30). Results are depicted next in figure 7.

One can easily notice, as a result of an impulsive start, how the leading-edge vortex segments travels away from the wing as number of time steps increases. Obviously, it takes about 30 time steps for the ***violent leading-edge vortices*** to ***completely clear out*** a trailing-edge wake with 18-segments long. Such a relationship can be used to determine the ***lag time*** when studying the aerodynamic interference of multi-lifting surfaces [8].

5.2.c Roll up of leading-edge wakes

Computations for the 3-rows bound mesh of the delta wing at angle of attack $\boldsymbol{\alpha = 20^o}$ are carried out. Figures 8(a) and 8(b) show the end view of the leading edge wakes only, without and with hidden-line removal, respectively. Figures 8(c) and 8(d) show corresponding rotational views.

In Fig. 8, the views depicted without hidden-line removal are not as clear as those depicted with hidden-line removal. The rotational views 8(b) and 8(d) show ***perfect visualizations of the leading-edge wake's roll up***. Furthermore, Fig. 8(b) shows very clearly the ***symmetric arrangement of the leading-edge-vortex*** system.

As the angle of attack increases this symmetric configuration becomes unstable which causes a loss of roll damping at small angles of roll. Consequently, any small disturbance introduced into the flowfield grows, and wing rock develops and hence the wing may enter into oscillatory rolling motion [2]. This phenomenon can be a major maneuver limitation and can pose a serious safety problem, specifically, when compact aircraft operate at subsonic speeds and high angles of attack.

Figure 9 below depicts the same views as in Fig. 8 but for the 6-rows bound lattice.

Again, the views depicted with hidden-line removal show ***perfect presentations of the leading-edge wake's roll up*** (Fig. 9b and 9d) and ***clear symmetric arrangement of the leading-edge-vortex*** system (Fig. 9b). The sharp edged elements in the later parts of the wakes are, most likely, produced by the fact that the freely moving wakes have strong influence on each other and hence very pronounced interference is produced.

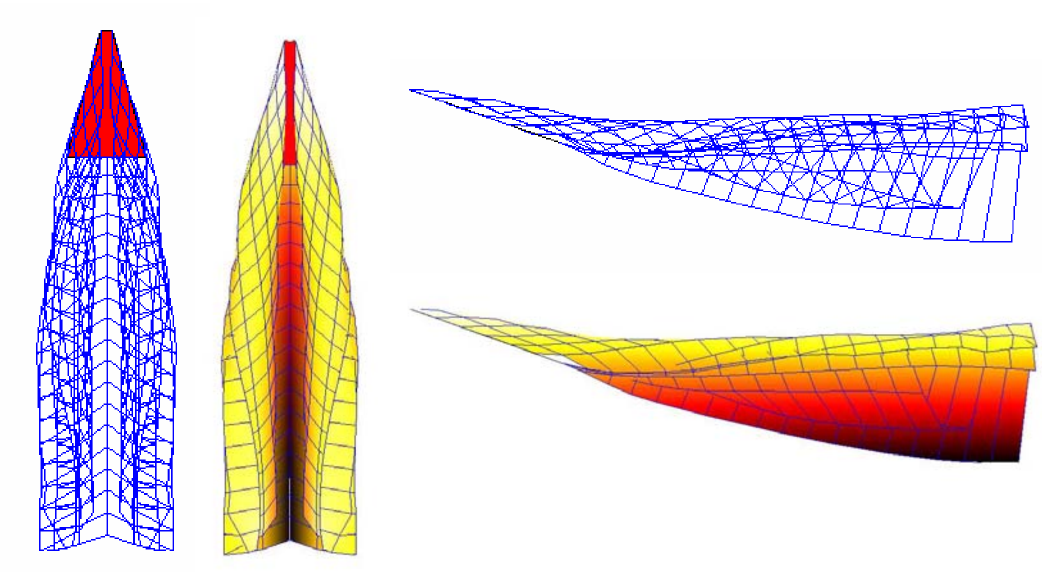

(6a) Top views (6b) Side views

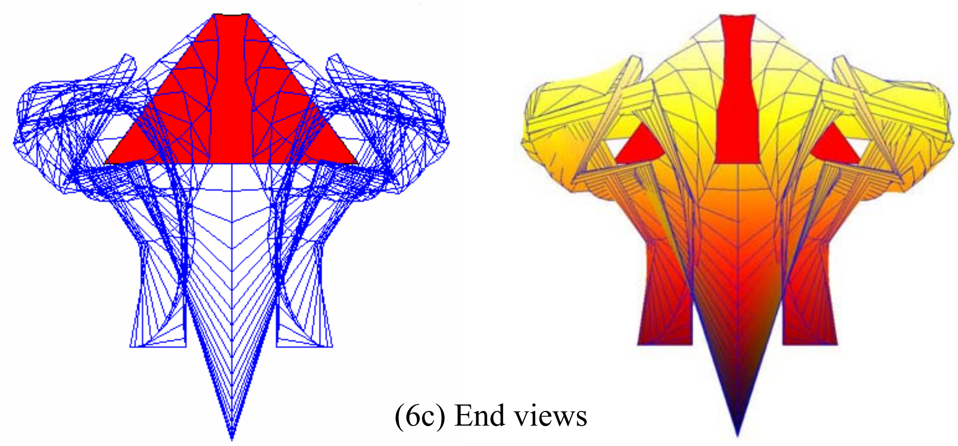

(6c) End views

Figure 6. Steady-state flowfield at angle of attack **$\alpha = 20^o$**

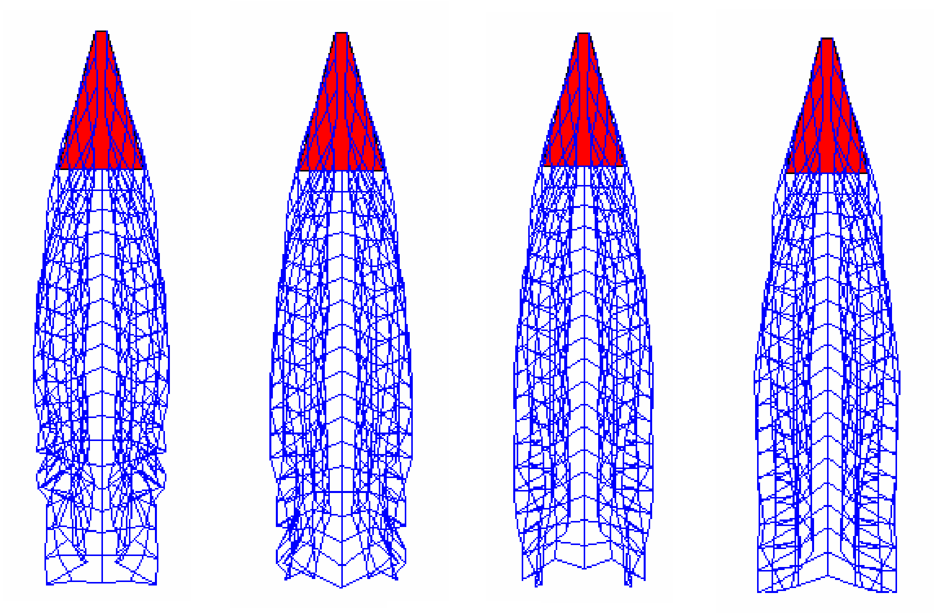

(7a)

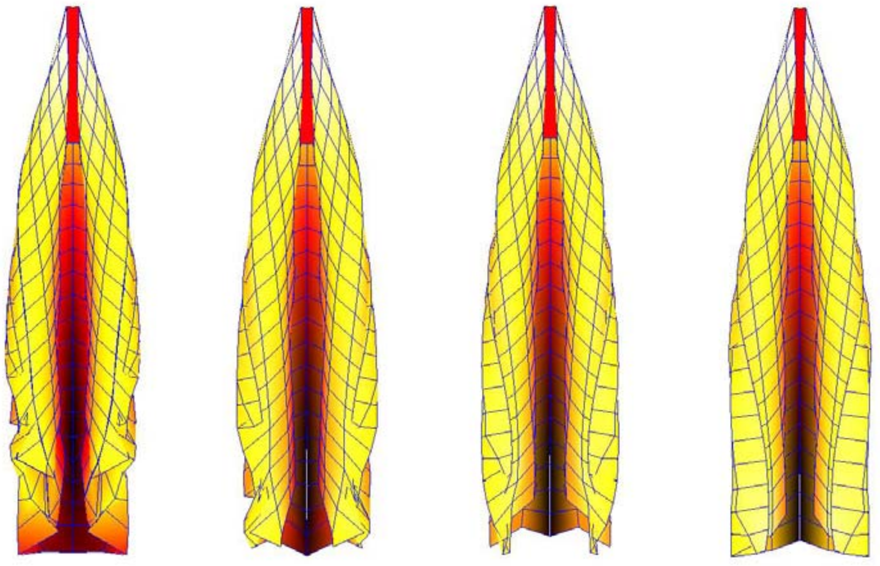

(7b)

Nsteps=21 Nsteps=24 Nsteps=27 Nsteps=30

Figure 7. Propagation of impulsive-start vortices: (a) without hidden-line removal, and (b) with hidden-line removal. Numbers of time steps are indicated.

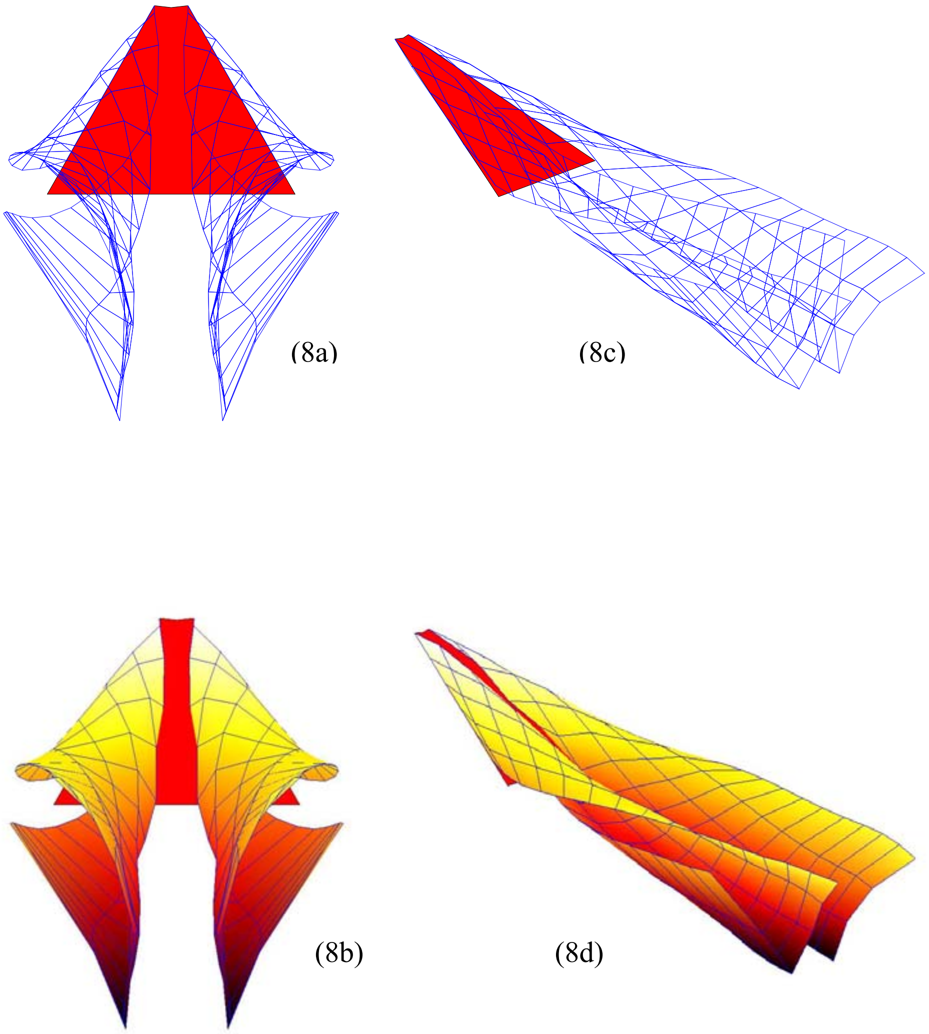

(8a) (8c)

(8b) (8d)

Figure 8. Leading edge wakes using 3-rows bound mesh:
(a) & (c): end and rotational views without hidden line removal
(b) & (d): end and rotational views with hidden line removal

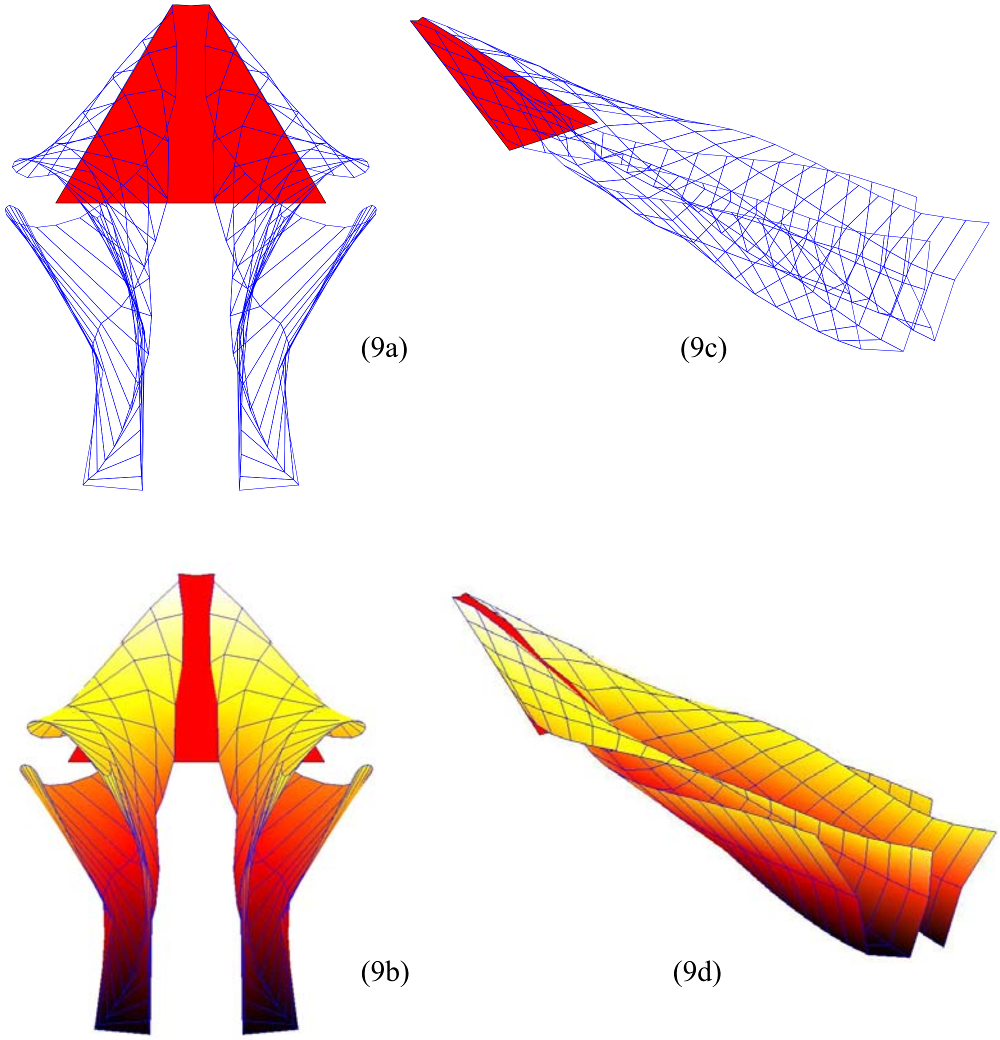

Figure 9. Leading edge wakes using 6-rows bound mesh:
(a) & (c): end and rotational views without hidden line removal
(b) & (d): end and rotational views with hidden line removal

5.2.d Influence of leading edge wakes on pressure distribution

To illustrate the influence of the leading-edge wakes on the pressure of the lifting surface, we plot the distributions of pressure differences (ΔCp) across the lifting surface for the 6-rows mesh at angle of attack $\boldsymbol{\alpha = 20^o}$. ***A cubic spline interpolation*** is applied through the pressure differences found at the control points (see Fig. 5). A separate cubic fit is applied through the results along the spanwise elements for each row, as shown in Figure 10.

Figure 10 indicates that ***high-pressure jumps*** exist in the front portion of the wing, i.e.; the wing lift force is largely composed of these pressure values. A careful comparison between Fig. 9 and Fig. 10 indicates that there is ***a strong downwash induced*** on the later portion of the wing, which is caused by the severe roll up of the leading-edge vortices.

Figure 11 shows a 3-D view of the two dimensional cubic spline interpolations across each row, which are basically the same results obtained in Fig. 10 but depicted in 3-D view.

Finally, we try a more complex task by considering pressure jumps, at all control points, and apply a ***3-D (surface) cubic spline interpolation***. Figure 12(a) shows the top view of such a surface fit, and Fig. 12(b) shows the end view for the same fit. Figure 12(a) also shows a “colorbar”, which is a color key for the values of the pressure difference.

Many advanced graphics features of MATLAB were used to produce the previous pictures. Color interpolation, shading, and light objects are some of the features that were used. Light object is placed at the top-left of the given views.
One can easily notice how well Figures 10 and 12(b) compare, however; Fig. 12(b) shows ***a more realistic visualization of the pressure distribution over the wing***.

6. Concluding Remarks

The present results illustrate the need for advanced graphics tools to accurately model the flowfields when simulating subsonic aerodynamic of lifting surfaces. Earlier investigations proved to have fallen short in responding to this need.

Powerful and sophisticated graphics tools such as hidden-line removal, color interpolations and shading, light objects, cubic spline interpolations, precise rotational techniques, and interactive plot editing, enabled us to ***significantly improve*** the graphical visualization of the subsonic aerodynamic of delta wings. More specifically, these tools enabled us to obtain the following:

a) Clear graphical visualization of the total flowfield over delta wings.
b) Distinctive graphical presentations for the roll up of leading edge wakes and their penetration of the trailing edge wakes.
c) Well-defined graphical presentations of the symmetric arrangement of the leading-edge-vortex system; which supports previous studies as to what causes the wing rock phenomenon.
d) Sequential pictorial presentations for the propagation of violent leading-edge vortices due to an impulsive start, witch emphasized the importance of lag time when studying the aerodynamic of multi-surface configuration.
e) Two and three-dimensional presentations of 2-D cubic spline interpolations of the pressure differences across spanwise elements of the bound lattice. This explained the composition of lift force.
f) Three-dimensional views of 3-D cubic spline interpolations of the pressure distributions; which produced very realistic visualization and hence more physical understanding.

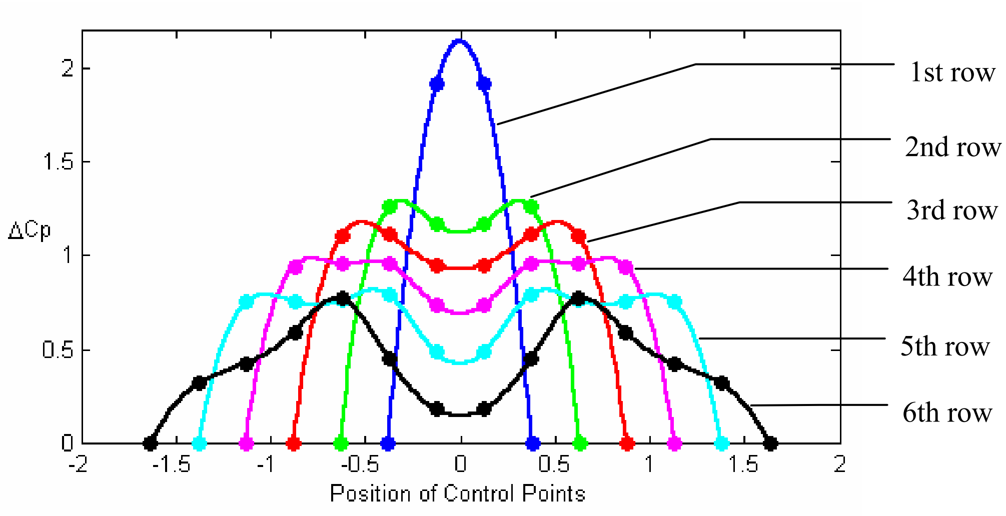

Figure 10. Variations of pressure differences across spanwise rows (6 rows)

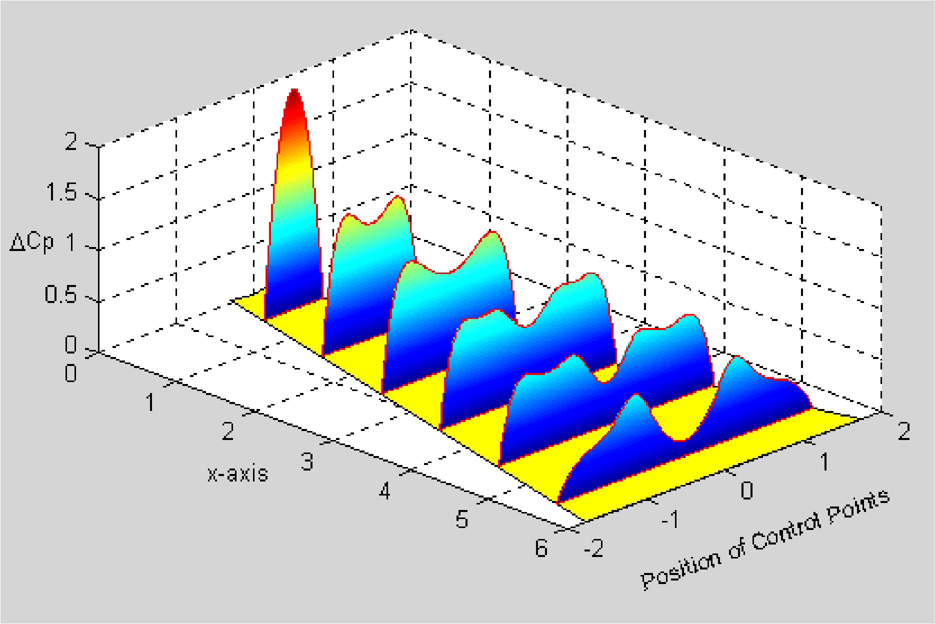

Figure 11. 3-D view for the 2-D cubic spline of the pressure differences

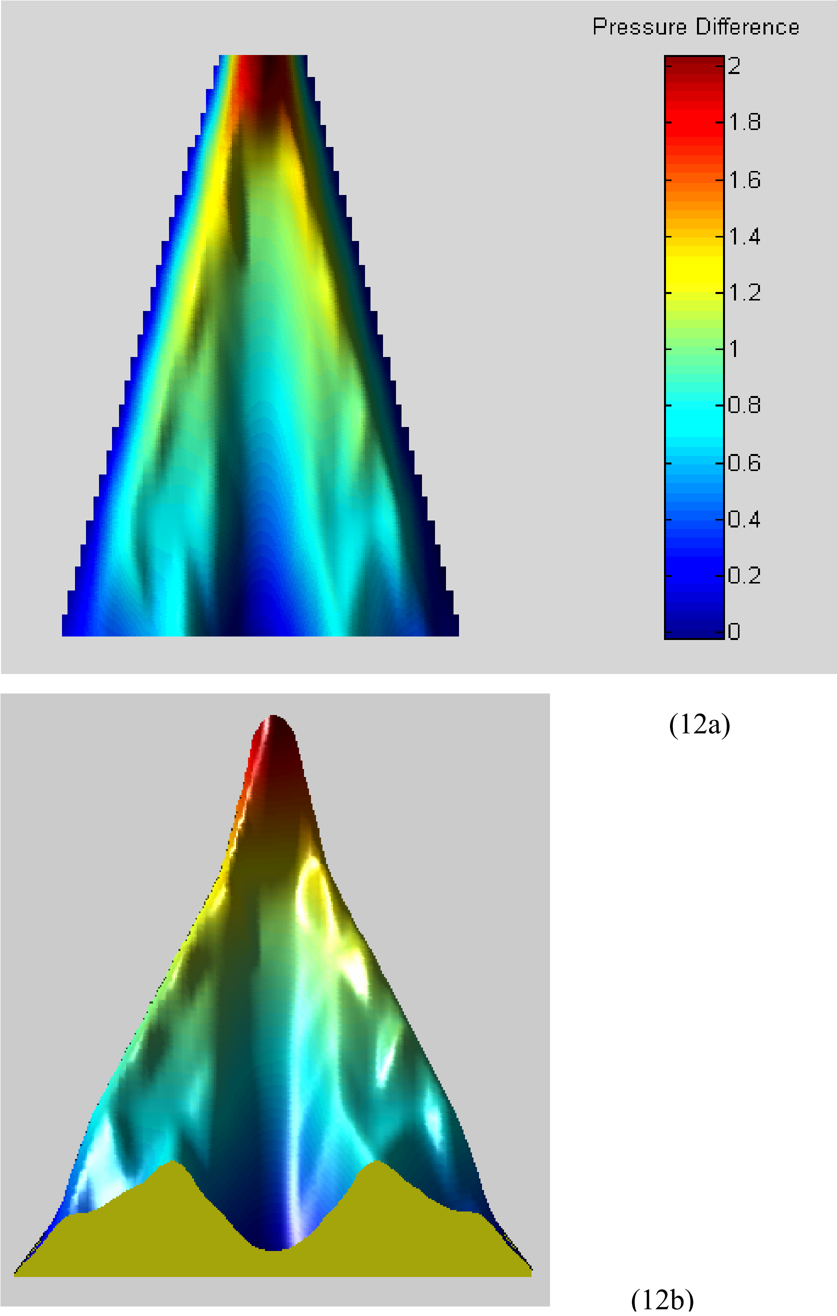

(12a)

(12b)

Figure 12: 3-D (surface) cubic spline of the pressure differences:
(a) Top view, (b) End view.

REFERENCES

1. Elzebda, J. M., "Two-degree-of-Freedom Wing Rock and Nonlinear Aerodynamic Interference," *Ph.D. Thesis*, Department of Engineering Science and Mechanics, Virginia Polytechnic Institute and State University, Blacksburg, Virginia, 1986.
2. Konstadinopouos, P., D. T. Mook, and A. H. Nayfeh, "Subsonic Wing Rock of Slender Delta Wings," *Journal of Aircraft*, Vol. 22, 1985, pp. 223-228.
3. Mook, D. T., and A. H. Nayfeh, "Application of the Vortex-Lattice Method of High-Angle-of-Attack Subsonic Aerodynamic," *SAE TP* 851817, 1985.
4. Nguyen, L. T., L. Yip, and J. R. Champers, "Self-Induced Wing Rock of Slender Delta Wing," *AIAA* Paper 81-1883, 1981.
5. Levin, D., and J. Katz, "Dynamic Load Measurements with Delta Wings Undergoing Self-Induced Roll-Oscillations," *AIAA* Paper 82-1320, 1982.
6. J. M. Elzebda, D. T. Mook, and A. H. Nayfeh, "Influence of Pitching Motion on Subsonic Wing Rock of Slender Delta Wings," *Journal of Aircraft*, Vol. 26, 1989, pp. 503-508.
7. Elzebda J. M., D. T. Mook, and A. H. Nayfeh, "Steady and Unsteady Aerodynamic Interference in Closely Coupled Canard/Wing Configurations." *Proceedings* of the Forum on Unsteady Flow Separation, the 1987 ASME Applied Mechanics, Bioengineering, and Fluids Engineering Conference, June 14-17; Vol. 52, 1987, pp. 37-44.
8. Elzebda J. M., D. T. Mook, and A. H. Nayfeh, "Numerical Simulation of Steady and Unsteady, Vorticity-Dominated Aerodynamic Interference," *Journal of Aircraft*, Vol. 31, No. 5, 1994, pp. 1031-1036.
9. Grafton, S. B., W. P. Gilbert, M. A. Croom, and D. G. Murri; "High-Angle-of-Attack Characteristics of A Forward-Swept Wing Fighter Configuration," *AIAA Paper* No. 82-1322, 1982.
10. Buchanan, T., and R. Cayse, "Aerodynamic Lag Investigation on the X029A at Mach 0.3 to 1.6," AEDC-TSR-86-V3, 1986.
11. "Getting Started with MATLAB," MATLAB 6, Release 12, the MathWorks, Inc., 2000.
12. Young W. Kwon, Hyochoong Bang, "The Finite Element Method using MATLAB," CRC Press, Inc., 1997.

13. "Using MATLAB," MATLAB 6, Release 12, the MathWorks, Inc., 2000.
14. "Using MATLAB Graphics," MATLAB 6, Release 12, the MathWorks, Inc., 2000.
15. Karamcheti, K., "Principles of Ideal Fluid Aerodynamics," John Wiley and Sons, Inc.,
    New York, 1966.
16. Kandil, O. A., T. Mook, and A. H. Nayfeh, "Nonlinear Prediction of the Aerodynamic
    Loads on Lifting Surfaces," *AIAA paper* No. 74-503, 1974.
17. Hummel, O., "On Vortex Formulation Over a Slender Wing at Large Angles of Incidence," AGARD CP-247, 1979.